RESEARCH ARTICLE

Fast Design of Spoke-Type PM Motor With Auxiliary Notches Based on Lumped-Parameter Magnetic Equivalent Circuit Model and Hybrid Multiobjective Optimizer

CONGDA XIAO [ID] [1], AIGUO HAN[1], WENLONG XIE[2], AND MINQI HE[1]
[1]School of Automotive Engineering, Wuhan University of Technology, Wuhan 430070, China
[2]Foshan Xianhu Laboratory of the Advanced Energy Science and Technology Guangdong Laboratory, Foshan 528200, China

Corresponding author: Congda Xiao (heshshaw@foxmail.com)

ABSTRACT The multi-objective design of PM motor is time-consuming. The accuracy complexity of the solver model and the efficiency of the optimizer affect the cycle of electromagnetic design. A fast design method of spoke-type PM motors with auxiliary notches based on lumped-parameter magnetic equivalent circuit (MEC) model and a hybrid multi-objective optimizer (HyMOO) are proposed in this article. The MEC model is established to quickly reflect the influence of design parameters on electromagnetic and torque performance in the account of auxiliary notch structure in the rotor lamination. Meanwhile, an HyMOO is proposed considering the Grey Wolves Optimization (GWO) model, to solve more complex multimode problems involving more parameters. The accuracy and high calculation speed of the proposed MEC are verified in comparison with the FE method. A benchmark test by general distance (GD) and inverted generational distance (IGD) proves the HyMOO with better converge speed and robustness. Based on the MEC model and HyMOO, a fast electromagnetic design is applied for the motor with requirements of 140Nm rated torque and 4.5% torque ripple. The optimal solutions are validated by FE analyses, and the best design are chosen, manufactured as prototype, and tested. Both the FE and experimental analyses verify the reliability of the fast design and the proposed motor.

INDEX TERMS Auxiliary notch, fast multi-objective design, multi-objective optimizer, lumped-magnetic equivalent circuit model, spoke-type permanent magnetic machine.

I. INTRODUCTION

Benefit from permanent magnets (PMs), PM synchronous machines (PMSMs) acquire higher efficiency, torque density, and a wider range of constant power operation [1], [2], which are extensively used as electric vehicle (EV) drive motors [3]. Among them, spoke-type PM synchronous machines can offer higher power densities owing to the magnetic concentration effect of rotor tangential magnetic circuits, which are suitable for limited space requirements of mini EVs [4]. Furthermore, with the use of FSCW, the power density is increased again while efficiency and cogging torque are

The associate editor coordinating the review of this manuscript and approving it for publication was Jinquan Xu [ID].

also improved, which amplifies the prominent merits of the spoke-type PM machine aforementioned [5]. However, there are drawbacks in traditional spoke-type PM motors, especially high torque ripple, low flux weakening capacity, and relatively high flux leakage ratio [6], which become the primary issues to be solved when spoke-type PM motors are used in mini EVs [7].

Meanwhile, due to the conflicts between design parameters on several performance indicators in the practical motor designing and optimization process, single-objective optimization methods can hardly meet the practical needs. For example, low torque ripple may always be obtained at the sacrifice of average torque [8]. Recently, various multi-objective optimization methods have been used in the design and

optimization of PM machines. Reference [9] proposed finite element (FE) based multi-objective large-scale design optimization method, and a Combined Multi-objective Optimization and Differential Evolution (CMODE) algorithm were used for the optimized parametric searching process. Though FE has proven highly accurate, the solution process consumes time and computational resources due to the complex FE model [10]. In [11], a Response Surface Methodology (RSM)-based method for experimental design with genetic algorithm (GA) was applied to multi-objective optimization. Using RSM as the solver of motor can greatly reduce the complexity of the mathematical model and allow the optimization algorithm to be subjected to less pressure [12]. However, the polynomial degree often does not represent the nonlinearity of solver model, and low approximation quality might lead to misjudgment [13]. Reference [14] offered a designing method for multi-objective deterministic and robust optimization using RSM and Multi-Objective Particle Swarm Optimization (MOPSO). The design for six sigma and Monte Carlo analyses were applied for further robust validation, which brought relatively convincing results, but a comprehensive and time-consuming process. Compared to the FE, the analytical model, such as magnetic equivalent circuit (MEC) model and sub-domain model, does have a considerable advantage in the computing process. Still, there is a problematic trade-off between computational accuracy and pre-maintenance workload [15], [16], [17]. Among the previous research, the study objects are generally consisting of a parametric solution model or a mathematical model that indirectly reflects the solution of multi-objective design and optimization. Few works has been done to offer the model a real computational time advantage and a high accuracy in quick design or pre-design. In addition, traditional multi-objective optimization algorithms such as Multi-Objective Evolutionary Algorithm (MOEA) or MOPSO for global optimization, are widely used in practical engineering problems with acceptable robustness but low search speed [18]. In another word, traditional optimizers may have convergence difficulties in multimode problems covering multiple inputs and outputs. Therefore, how to design and optimize the machines' design parameters fast to meet multiple variable performance requirements in a short time and meanwhile with guaranteed accuracy becomes a vital issue.

In this paper, a lumped parameter magnetic equivalent circuit (MEC) model based on a 16-pole 18-slot spoke-type PM FSCW motor with auxiliary notches for mini EV is presented. The MEC model with the ability to capture essential effects, including stator slot leakage, core saturation and moving air-gap, is designed to solve and analyze the proposed machine's general performance in an early design stage. Besides, a new Hybrid Multi-Objective Optimizer (HyMOO) based on the proposed Enhanced Multi-Objective Grey Wolf Optimization (EMOGWO) algorithm and MOPSO is developed with fast convergence and good robustness, to make the optimization more efficient in the complex MEC solver. With the combination of MEC model and HyMOO, the multi-objective

design process shows high efficiency and high accuracy, and solves the problem of rapid and stable optimization design that meets the design requirements of the proposed machine in the early stage of the project.

The rest of the article begins with a description of the machine topology, design requirements, and performance specifications in Section II. In Section III, an original FE model, MEC and parametric chart, including special structural designs, are developed. The baseline comparison results with FE model are presented according to the requirement of analyzing the electromagnetic performance characteristics of machine fast and accurately. The development of EMOGWO and HyMOO result in Section IV, as well as the verification benchmarks of optimizer performance. Section V carries out the multi-objective designing for machine's torque performance, including establishing parameter constraints based on design requirements and the mechanical structure of machine topology. The resultant solutions are testified by FE analysis and prototype experiments in Section V. Section VI draws a conclusion to the article.

II. INITIAL MACHINE TOPOLOGY AND SPECIFICATION

The proposed FSCW spoke-type PM motor is a 16-pole/ 18-slot design, and its cross-section is shown in Fig. 1. The tangential magnetic circuit design of rotor provides a significantly enhanced magnetic concentration effect, while FSCW has a lower slot-per-pole ratio than distributed winding, which significantly improves the air-gap magnetic density and increases the average torque. Compared to conventional spoke-type PM motors or derivations with eccentric poles used by previous study [6], [17], [19], the machine has auxiliary notches (ANs) to adjust the rotor magnetic circuit and linearly changes part of the air-gap length along the circumferential direction, equivalently adjusting the air-gap magnetic density to make it more sinusoidal, thus reducing harmonics (Fig. 1(a)). Meanwhile, the notch structure optimizes the magnetic concentration effect and reduces manufacturing accuracy requirements compared with eccentric poles.

At the same time, to further weaken the potentially harmonic-related problems caused by FSCW, a four-layer concentrated winding layout is applied. Compared with double-layer winding, the four-layer winding, based on the advantage of spatial misalignment, can reduce both the sub- and super-stator magneto-motive force (MMF) harmonics by further stacking the number of winding layers per slot. As shown in Fig. 1(b), each phase has three positive and three negative sectors, and the back-EMF is proven to be more sinusoidal with less total harmonic distortion (THD) [20].

In addition, another combination of ANs is set at the inner edge of the rotor lamination, right in the middle of two adjacent PMs, to further modify the rotor magnetic circuit, reduce flux leakage and maximize PM utilization.

The specifications of pre-design are demoed in Table. 1. The main stator/rotor lamination factors and winding specifications have been constrained by the space or mechanical
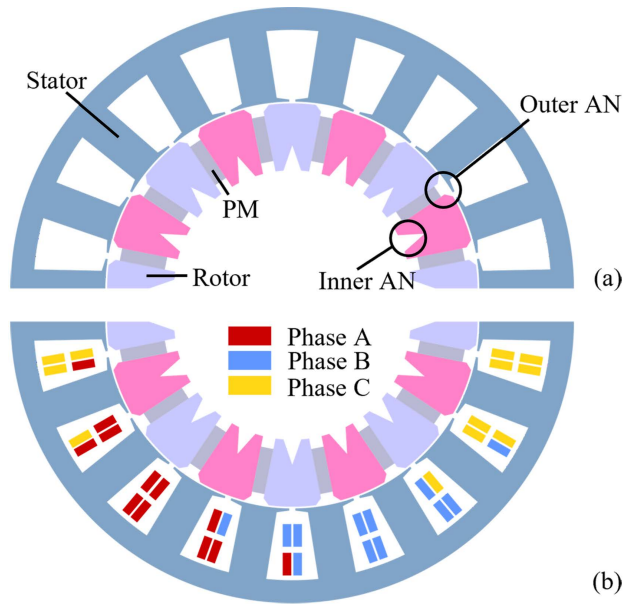
FIGURE 1. Machine topology illustration. (a) Cross-section of proposal machine. (b) Winding pattern of proposal machine.

TABLE 1. Units for magnetic properties.

Parameters	Value	Unit
Stator outer/inner diameter	270/179.3	mm
Rotor outer/inner diameter	177.6/60	mm
Air-gap	0.85	mm
Lamination stack length	70	mm
Phase	3	-
Turns	11	-
Parallel paths	4	-
Rated power	40	kW
DC link voltage	340	V
Rated current	141	Arms
Rated torque	140	Nm
Rated speed	3000	rpm
Torque ripple	<4.5%	-

constraints and initial experimental calculations. The designing and optimization objective is to ensure that the average of rated torque meets the requirements while achieving optimum value for torque ripple.

III. FE AND MEC MODEL DESCRIPTION

In order for simplifying the computational difficulties of the model, both the baseline FE and MEC models were built based on the following assumptions,

1) Spoke PMs are tangentially magnetized with linear demagnetization characteristics.
2) End effects and eddy current influence are ignored.
3) Magnetic leakage along axial direction at both ends of laminations is ignored.
4) The structure of retaining sleeves is ignored.

Hence, the 3-D machine structure can be simplified to a 2-D model, and some of the weakly influenced structures can be approximated.

A. BASELINE PARAMETRIC FE MODEL

To ensure the accuracy of the baseline FE model, the model consists of 27266 cells, where the air gap section is divided into 3 layers along tangential direction to capture the massive air gap magnetic flux density distribution of the proposal spoke-type FSCW PM motor. Fig. 2 shows the rotor configuration and design variables of the target parametric model topology. 10 design parameters need to be rationally considered and optimized. w_m and h_m are the thickness and length of the PM, respectively, h_{mo1} and h_{mo2} are the length of the PM outer and inner offset, α_1 is the electric angle between the ends of two adjacent outer ANs, α_2 is the electric angle between the ends of the inner AN, h_{n1} and h_{n2} are the length of the outer and inner AN respectively. R_{ro} is the rotor outer radius obtained from the initial design specification.

B. MEC MODEL

The development of the Magnetic Circuit Model (MCM) is based on the magnetic flux pattern of study object. During the analytical design of the PM machine, the machine structure was divided into several main lumped permeances, flux sources and MMF sources elements for approximate calculations based on the flux paths and the relative spatial-temporal positions of each phase armature winding and PMs. The governing equation at each lumped element is given as:

$$\Phi = P * F \tag{1}$$

where, Φ, P and F are magnetic flux, permeance, and MMF, respectively. In general, difficulties are found for MCMs to accurately approximate the on-load operating conditions of interior permanent magnet (IPM) machines without magnetic barriers constrained, in that the varying q- and d-axis fluxes generated by armature winding excitation cause unpredictable distortions in the rotor flux pattern. However, as shown in Fig. 3(a)(b), in the spoke-type PM motor proposed here, the rotor magnetic flux path is limited by a strong magnetic concentration effect as well as both outer and inner ANs, which a well-designed MCM can accurately predict. To simplify the modelling and calculation process, the MEC model uses a 1/2-cell unit of the original 16-pole/18-slot design which consists of 8 units of rotor pole, 9 units of stator tooth and a combination of adaptive air-gap units (Fig. 4). In the pictures, air linear permeances, PM linear permeances, nonlinear permeances, PM flux sources and winding MMF sources are represented by different symbols and adjacent elements are connected by sequential nodes. All permeances can be calculated using the following equation.

$$P = \frac{\mu_0 \mu_i A_i}{L_i} \tag{2}$$

in which A_i is the area flux passing through, L_i is the length in flux direction, μ_0 and μ_i are the air permeability and relative permeability, respectively.

All elements are interconnected by nodes to form a nodal network system, calculated by applying Kirchhoff's law.
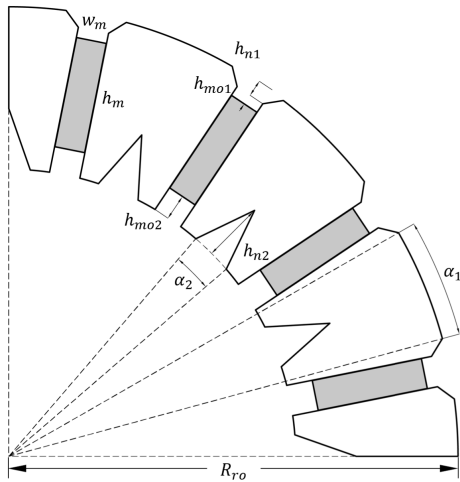
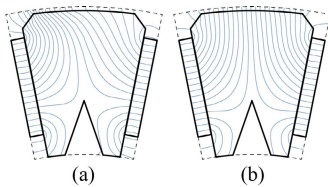**FIGURE 2.** Rotor parametric construction of the proposal machine.

FIGURE 3. Rotor flux path of the proposal machine. (a) I_{rms} = 210Arms, γ = 50°. (b) I_{rms} = 210 Arms, = 0°.

☐ Air Linear Permeance
🟥 PM Linear Permeance
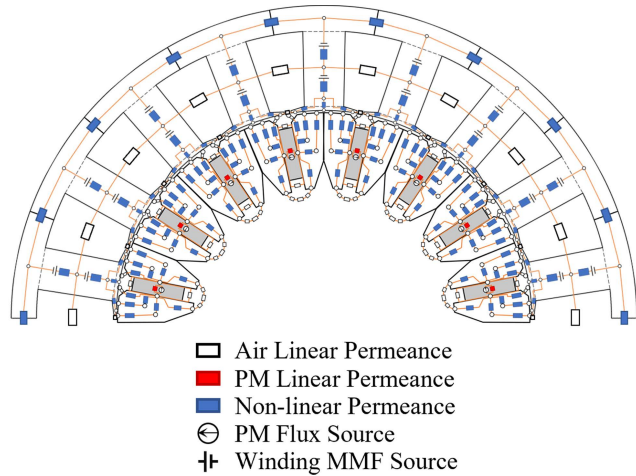🟦 Non-linear Permeance
⊖ PM Flux Source
⊣⊢ Winding MMF Source

FIGURE 4. Proposed MEC model for the machine.

Descriptions of the main components modeling are presented in the following subsections.

C. STATOR UNIT FOR MEC
In FSCW machines, the lower slot-per-pole ratio results in a large number of saturated areas in the stator teeth, especially in the tooth tips, so leakage in the stator slots and tooth tips needs to be taken into account. In Fig. 5, the modelling of
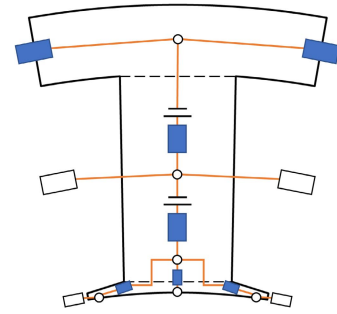

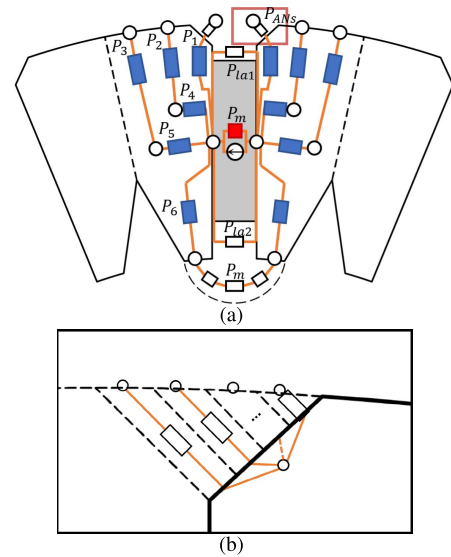**FIGURE 5.** Specification of stator magnetic circuit model.

FIGURE 6. Specification of rotor magnetic circuit model. (a) Single rotor pole. (b) The outer AN.

the stator unit is divided into four main sections, namely the stator yoke, teeth, tooth tips and slots.

The yoke consists of one non-linear permeance element. A tooth tip unit is subdivided into three non-linear permeance elements and two air linear permeance elements. The elements form nodes at the junction with the air-gap, respectively, to capture flux paths and leakage accurately.

The MMF generated by the armature winding can be calculated by,

$$F_{wi} = N_w I_i \qquad (3)$$

where, N_w and I_i are the number of turns and phase current, respectively. The tooth is split into two parts so that each winding of the four-layer winding form can be represented by the corresponding MMF source and a non-linear permeance element in series. Finally, the leakage in the slot is calculated by a single air linear permeance element connected to the central node of the adjacent tooth, respectively.

D. ROTOR UNIT FOR MEC
To approach the actual situation, the non-linear flux elements of the rotor core are divided into more parallel branches in

various shapes based on the spatial dimension of the flux path, while the previously mentioned parameters to be optimized need to be accurately expressed in these elements.

According to the results shown in Fig. 3, the flux in the rotor is divided into three main flux paths interconnected to the air gap region and three leakage flux paths in parallel with each other, as shown in Fig. 6(a). The permeance values are explained as follows:

$$P_1 = \frac{\mu_0 \mu_1 L w_1}{h_{n1}} \log\left(\frac{h_1 + h_{mo1}}{h_{mo1}}\right) \tag{4}$$

$$P_2 = \frac{\mu_0 \mu_2 L (\alpha_1 R_{ro} + 4w_2)}{8(h_2 - h_{n1} - h_{mo1})} \log\left(\frac{h_2}{h_2 + h_{mo1}}\right) \tag{5}$$

$$P_3 = \frac{\mu_0 \mu_3 L(\alpha_1 R_{ro} + 4w_3)}{8(h_3 - h_2)} \log\left(\frac{h_3}{h_2}\right) \tag{6}$$

$$P_4 = \frac{\mu_0 \mu_4 L (h_m + h_{mo2} - h_{n2})}{2(w_4 - w_1)} \log\left(\frac{w_4}{w_1}\right) \tag{7}$$

$$P_5 = \frac{\mu_0 \mu_5 L (h_m + h_{mo2} - h_{n2})}{2(w_5 - w_4)} \log\left(\frac{w_5}{w_4}\right) \tag{8}$$

$$P_6 = \frac{\mu_0 \mu_5 L (w_5 - w_6)}{h_{n2} \cdot \log\left(\frac{w_5}{w_6}\right)} \tag{9}$$

$$P_{la1} = \frac{\mu_0 L h_{mo1}}{w_m} \tag{10}$$

$$P_{la2} = \frac{\mu_0 L h_{mo2}}{w_m} \tag{11}$$

$$P_{le} = \frac{8\mu_0 L}{\pi} + \frac{\mu_0 L w_6}{w_m} \tag{12}$$

$$P_m = \frac{\mu_0 \mu_r L w_m}{h_m} \tag{13}$$

where, w_i and h_i represent the width and height of corresponding area for P_i ($i = 1, 2, \ldots, 6$), L represents the axial length of lamination stack.

Further, the unequal length of the air-gap caused by the outer ANs needs to be considered. In Fig. 6(b), the outer AN area as referred is divided into s_{max} parallel air linear flux elements of equal length along the radial direction, and form nodes at the junction with the air-gap, respectively, expressed by:

$$\begin{cases} P_{ANs} = \frac{\mu_0 L}{4s_{max}} \sqrt{4{h_{n1}}^2 + {w_m}^2} \log(\frac{s+1}{s}) \\ s = 1, 2, \ldots, s_{max} \end{cases} \tag{14}$$

E. AIR GAP MODELING

Due to the massive air-gap flux density of the FSCW machine, especially the proposal spoke-type pattern with equivalent uneven air-gap length, the magnetic density of the air gap region needs to be captured precisely. Based on the independent distribution of each unit in this MEC model and the node network connection, an adaptive multi-layer air-gap modelling method proposed in [21] is considered here. The air-gap is first divided into quantities of two-layer radial air linear elements by interconnections of rotor- and stator-side nodes, each rotor-side network node is connected to a
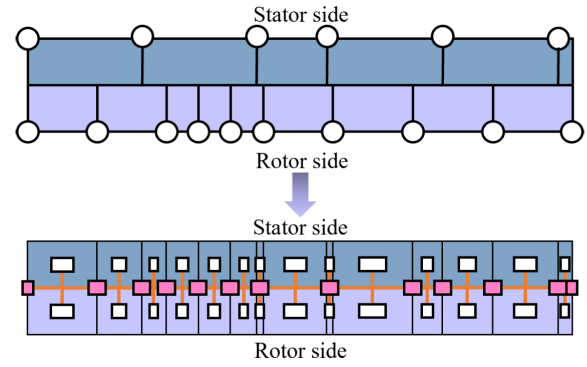
minimum of two nodes on the stator side, and the complementary condition is proper for each stator-side node. Then, the adjacent nodes in the middle of two radial elements are connected using the permeance in circumferential direction, respectively (Fig. 7). This division requires the model to be updated in real-time during the calculation process based on the relative physical positions of the rotor and stator; the increase in calculation time is inevitable but enables fine approximation to be made.

F. MEC CALCULATION

The iterative calculation flowchart of MEC model is shown in Fig. 8. First, the nodal system and element calculation functions are initialized according to the design specifications, operating conditions, and parameter values to be optimized for the machine. A structure array is created to track the MMF of the node network and the relative permeability of each permeance element [22]. In combination with this structural array, the permeance and flux matrices are built and used to calculate the MMF matrix at each iteration. After that, the relative permeability fit values of the non-linear permeability elements can be calculated by interpolation of the BH curve of materials and basic equations below:

$$\mu_r [i + 1] = \mu_r [i]^{0.05} * \mu_{rf} [i]^{0.95} \tag{15}$$

where μ_r and μ_{rf} represent the former and fit value of element permeability. The nonlinear iterative calculation continues until μ_r converges to within a set tolerance, after which the relevant results are recorded, and the model is reinitialised to start the next set of calculations.

G. MEC RESULTS AND VALIDATION

To validate the accuracy and calculation speed of the proposed MEC model, the calculation results were compared with the FE model results and computational time for an original sample in Fig. 1. The validation was carried out mainly from open-circuit characteristics, on-load characteristics calculation, and processing time. The environment of MEC model was chosen to be Python 3.9, and the device was an AMD Epyc-7601 32-core processor with 60GB of RAM.
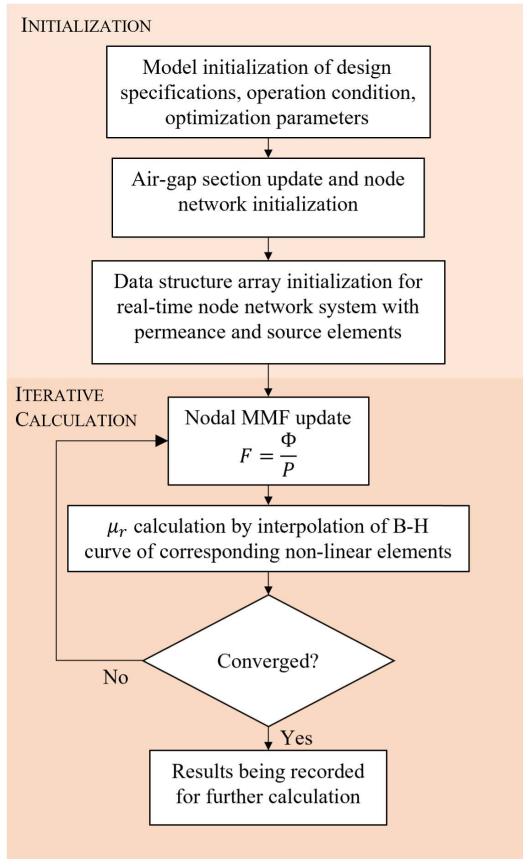
FIGURE 8. Flowchart for MEC calculation.

FIGURE 9. Comparison of air-gap flux density. (a) radial. (b) circumferential.

FIGURE 10. Comparison of flux-linkage.

The MEC model uses a discrete parallel computing bundle of 32 consistent with the number of processor cores, and the FE model is set up in a commercial software for the most efficient operating environment as well.

1) OPEN-CIRCUIT CHARACTERISTICS

Fig. 9(a) and (b) provide the calculation results of the radial and circumferential flux density traces, respectively, where traces with solid lines represent MEC results and traces with dotted lines represent FE model results. The MEC computed circumferential flux density waveform is slightly coarser than the FE model due to the local saturation of core edge. However, it can still accurately calculate the peak flux density and the waveforms are generally consistent.

Fig. 10 and Fig. 11 show the calculated waveforms of the flux linkage and back EMF of phase A for both models at 1000 rpm. The MEC waveform looks good in comparison with the FE and accurately reflects the open-circuit electromagnetic characteristics of the machine.

Fig. 12 shows the calculated waveform for cogging torque over a certain period which will be important when evaluating the machine torque performance. The two waveforms are similar, especially at the peak points, and some of the errors that occur in the MEC result do not affect the visual evaluation of performance.
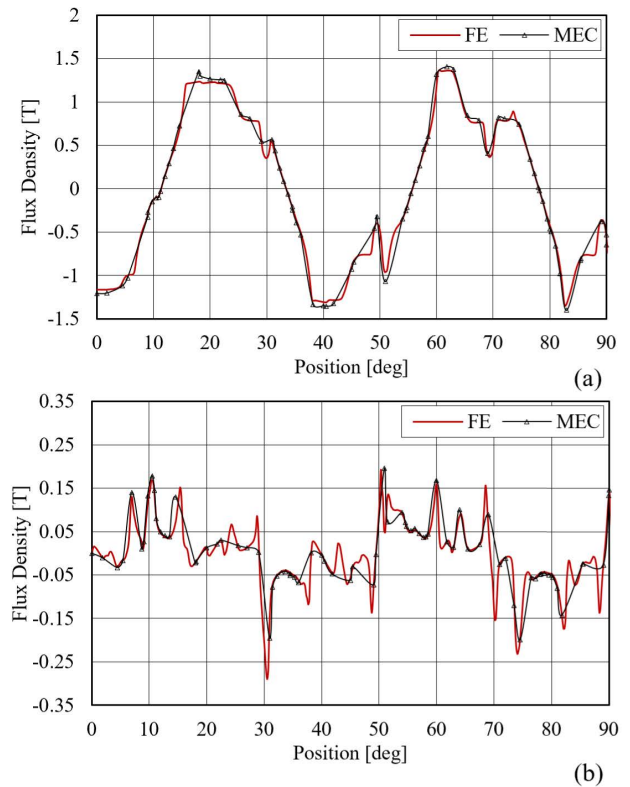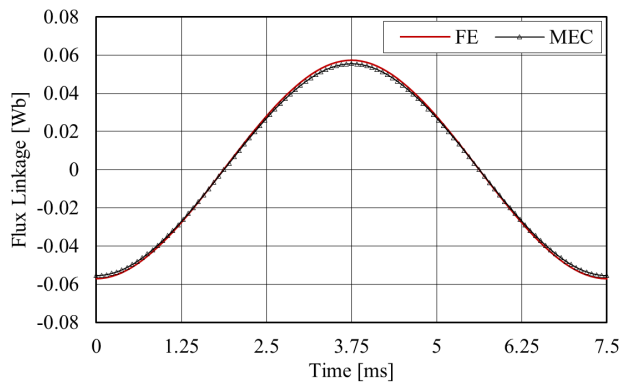
In summary, the MEC model is fully capable of meeting the computational accuracy of the open-circuit characteristics of the proposed machine.

2) ON-LOAD CHARACTERISTICS

Fig. 13 shows the comparison of torque waveforms of MEC and FE calculations under an on-load condition of 1500 rpm for rotor rotation in the presence of 100Arms for stator current. The two waveforms maintain matched, where the magnitude error is within 5%.
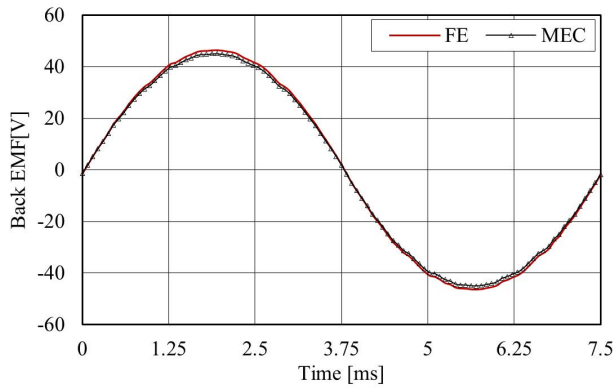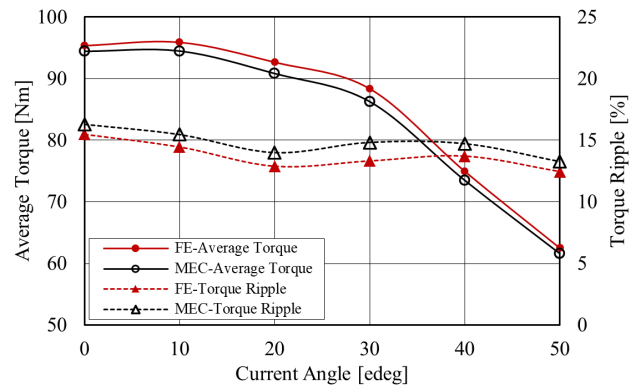
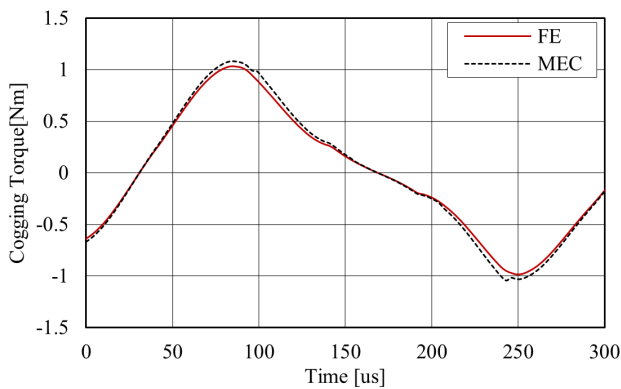**FIGURE 11.** Comparison of back-EMF.

FIGURE 12. Comparison of cogging torque.

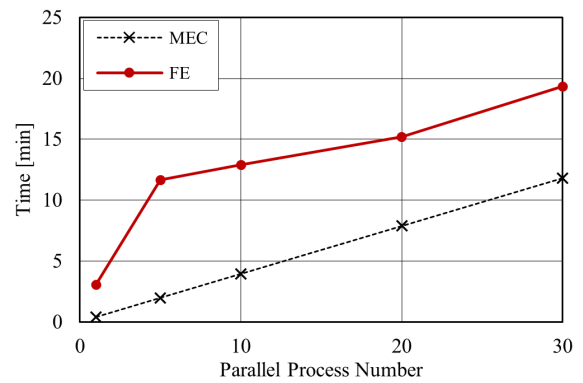**FIGURE 13.** Comparison of torque output.

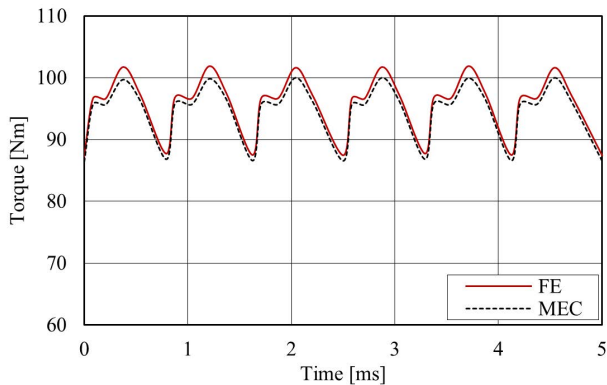**FIGURE 14.** Comparison of torque output.

FIGURE 15. Comparison of torque output.

Fig. 14 shows the calculated values of average torque and torque ripple for the stator current angle varied in experimental range $\gamma \in [0, 50]$ by MEC and FE analysis. The MEC calculations basically match the FE for the whole range of current angles and the errors are negligible.

Thus, the proposed MEC model can accurately predict the torque performance of the corresponding machine design under on-load conditions.

H. PROCESSING TIME COMPARISON

Table. 2 shows the comparison of processing time in the prementioned subsections by the proposal MEC and FE model, respectively. In single-step calculation, the MEC model requires less than 13% of processing time compared with FE. In 60-step calculation for one electrical cycle, the final time is still significantly ahead of the FE model with calculation speed that is about 22 times faster than FE, even though the discrete calculation approach and data processing causes the parallel MEC process to lose some time.

Fig. 15 shows the processing speed performance of the proposal MEC and FE model in multi-process calculation. The processing time of FE increases significantly due to the intervention of parallel computing; the proposed MEC model uses linear logic in the multi-process calculation, thus the processing time increases linearly.

With smaller computational resources, the proposed MEC model has a massive speed advantage over FE, with a 78% reduction in processing time compared to FE for a maximum parallel computation of 30; at the same time, the results of the MEC model are very close to FE under various load conditions, and the errors can be neglected in fast design.

Thus, the MEC model is proven to be a good combination of computational speed and computational accuracy.

TABLE 2. Processing time.

Load condition	Single-step time [s]		60-step time [s]	
	MEC	FE	MEC	FE
Open-circuit	2.34	22.90	8.19	209.16
On-load	2.47	20.15	8.31	183.12

IV. DEVELOPMENT OF HYMOO

The significance of multi-objective optimization in engineering is to obtain the Pareto optimal solution set from all the solution vectors of the problem and select robust designs from the actual situation [23]. According to this feature, various single-objective natural heuristic optimization algorithms evolve into multi-objective optimization algorithms, such as MOEA [24] and MOPSO [25], which are widely used.

Whether in this paper or other practical engineering optimization problems, the calculation of objective function value occupies most of the computing resources and time. Obtaining accurate and optimal results in less time with limited computing resources is the key to improving optimization efficiency. Therefore, for the optimizer, when the number of parallel computing processes is constrained, representative solutions should be obtained with the least iterations.

Like the above meta-heuristics, the MOGWO algorithm inherits the fast convergence characteristics of the grey wolf optimization (GWO) algorithm [26], which is precisely what is needed in multi-objective machine design and optimization, but it is extremely easy to fall into local optimum [27]. Some efforts have been made without the possibility of practical application in engineering problems [28]. To improve the shortcomings of MOGWO algorithm and highlight the advantages of its convergence efficiency, a hybrid optimizer using EMOGWO algorithm with MOPSO assisted is proposed and verified.

A. BRIEF DESCRIPTIONS OF MOGWO ALGORITHM

The basic idea of MOGWO is still inherited from GWO, which is inspired by the natural phenomenon that the leader wolves always lead the whole wolves during hunting. Here is the optimization process of the algorithm:

Consider each individual in the population as a solution and obtain three of the most dispersed solutions from the Pareto optimal solutions as leaders α, β and δ respectively. The individuals eventually approach the global optimal solution under the guidance of the three leaders. The specific guiding equations are as follows:

$$D_p = C \cdot X_p(t) - X(t) \tag{16}$$

$$X(t+1) = \frac{1}{3} \sum_{p=\alpha,\beta,\delta} (X_p(t) - A \cdot D_p) \tag{17}$$

where, X is the individuals' position, X_p is the leaders' position, t is the iteration number. A and C are guiding coefficient

calculated by,

$$\begin{cases} A = 2a \cdot r_1 - a \\ C = 2r_2 \end{cases} \tag{18}$$

where, both r_1 and r_2 are random values in [0, 1], a is the control factor in [0, 2] linear increasing with the iteration number.

B. DEVELOPMENT OF EMOGWO

Given the above MOGWO problems and combined with the actual application requirements, EMOGWO is proposed based on the following detailed improvements.

1) LOCAL BEST STRATEGY

When MOGWO runs, it can be observed that individuals are too blond to the leader because they do not have their own cognitive ability, abandoning the possibility of individual tracking the local optimal solution, and become one of the key factors that lead to the algorithm easy to fall into local optimum. Inspired by the MOPSO algorithm, the local best position of each individual is recorded and introduced into the guiding (19), and the influence intensity is adjusted by the weight coefficient σ, which is expressed as follows:

$$X(t+1) = \frac{1-\sigma}{3} \sum_{p=\alpha,\beta,\delta} (X_p(t) - A \cdot D_p) + \sigma (X_{pbest}(t) - A \cdot D_p) \tag{19}$$

where X_{pbest} represents indivisuals' local best position. In anticipation, the introduction of local best is more feasible for enhancing the individual exploration ability and adjusting the head guidance strength according to the pre-set value.

2) NON-LINEAR CONTROL FACTOR

In the original MOGWO algorithm, the control parameter increases linearly with the iteration, and the exploration intensity of the algorithm decreases. The application of nonlinear control parameter a in the GWO algorithm is discussed in [29], and it is also applicable in multi-objective algorithms. Under the premise of lack of exploration ability, a is adjusted to power function form, expressed as:

$$a = 2 - 2 \left(\frac{t}{t_{max} \cdot (1 + t_f)} \right)^k \tag{20}$$

where t_{max} is the maximum iteration value, t_f is the compensation iteration value in [0, 0.5], and k is a rational number greater than 1. Specifically, t_f is used to adjust the response delay of function a to t, and k is the exponent of the power function, which two jointly affect the convergence speed and exploration ability of the algorithm. The larger values of t_f and k can improve the searching ability of the algorithm in the pre- and mid-iteration period.

C. DEVELOPMENT OF PROPOSED HYMOO

1) IMPLEMENTATION OF MOPSO

On the premise of keeping the total number of individuals consistent, a relatively independent efficiency population is introduced, which accounts for 1/3 of the total. This population will execute the MOPSO algorithm, and the others will execute the EMOGWO algorithm, which is called the converge population. The two populations share the same Pareto archive, which gives play to both MOGWO in convergence speed and MOPSO in search advantages.

2) RANDOM SEARCHING

After each iteration in the optimization process, there should be no individuals with duplicated or over-approximate design parameters. This is not only easy to lead individuals to an extreme point, but also takes up unnecessary computing resources in practical projects. Therefore, the algorithm adds the process of screening aggregation individuals and random searching, in which screening is followed by searching. If and only if:

$$
\begin{aligned}
&\left[\forall i, j \in \{1, 2 \ldots, pop\}, X_i = X_j\right] \cap \\
&\left[\exists i, j \in \{1, 2 \ldots, pop\}, \left|X_i - X_j\right| \le X_{tol}\right]
\end{aligned} \quad (21)
$$

where pop represents the population of all individuals, X_{tol} is the tolerant difference array, for X_j satisfying (21) will be reset before the objective function is calculated as the descriptions below:

$$
\begin{cases}
\boldsymbol{x}'(x_1', x_2', \ldots x_i', \ldots, x_{dim'}) = \left\{x_i' = r \cdot (x_{ub_i} - x_{lb_i})\right\} \\
X_j = X_j + \boldsymbol{x}'
\end{cases} \quad (22)
$$

where dim is the dimension of X, r is a random value in $[-0.3, 0.3]$, x_{ub_i} and x_{lb_i} represents the upper and lower boundary of x_i respectively.

In summary, this random search step will greatly reduce repeated or similar calculations and save computing resources. Meanwhile, the population can break away from local optimum, which enables the algorithm's exploration capabilities to be enhanced, speeding up the process of finding the complete Pareto front.

The main process of the HyMOO is shown in Fig. 16.

D. OPTIMIZER PERFORMANCE VERIFICATION

To test the actual performance of algorithms, the HyMOO is compared with the original MOGWO and MOPSO algorithm for simulation verification.

1) BENCHMARK FUNCTION AND INDICATORS

The benchmark functions were chosen from the UF multimode test suite [30] for UF2 and UF4, where UF2 and UF4 are two-objective test problems while both have many local optimal solutions.

A relatively generic performance indicator, Generational Distance (GD), is used as an evaluation criterion for algorithm
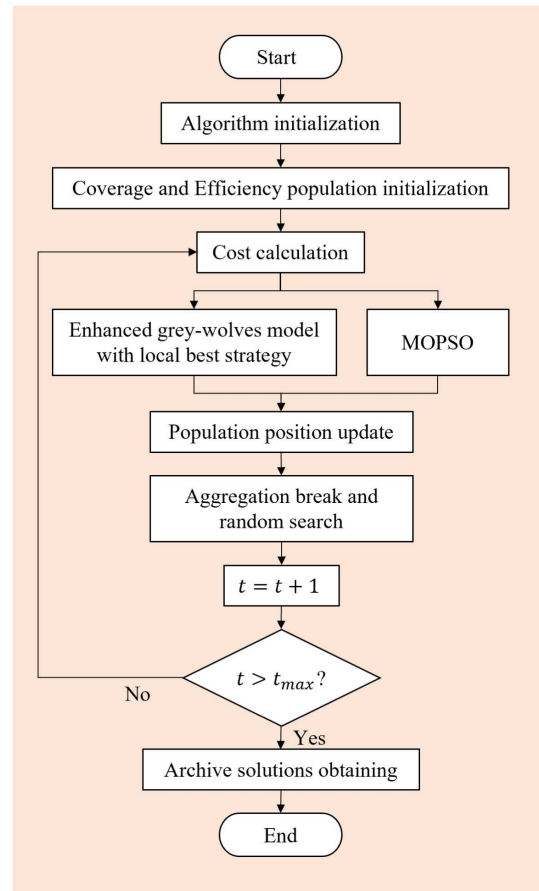

FIGURE 16. Flowchart for the proposal HyMOO.

validation, calculated as follows [31].

$$
GD(S) = \frac{1}{|S|} \sum_{z \in S} \min_{z' \in P_s} \left\{d\left(z, z'\right)\right\} \quad (23)
$$

where S is the resultant solutions of optimization algorithm, P_s is the real Pareto front of objective function. GD accurately reflects the convergence of the optimization results, with lower GD values representing more reliable results, which is suitable for verifying the accuracy of a multi-objective optimization algorithm that needs to be applied in practical engineering.

Meanwhile, another performance indicator Inverted Generational Distance (IGD) is considered here [32],

$$
IGD(S) = \frac{1}{|P_s|} \sum_{z' \in P_s} \min_{z \in S} \left\{d\left(z, z'\right)\right\} \quad (24)
$$

IGD represents the inverse mapping of GD to reflect the distribution of optimization results on the real Pareto front. A multi-objective optimization algorithm with fine robustness can always obtain the resultant solutions with high diversity and lower IGD value. Combining IGD and GD, the optimization and convergence effect of the algorithm can be well evaluated.
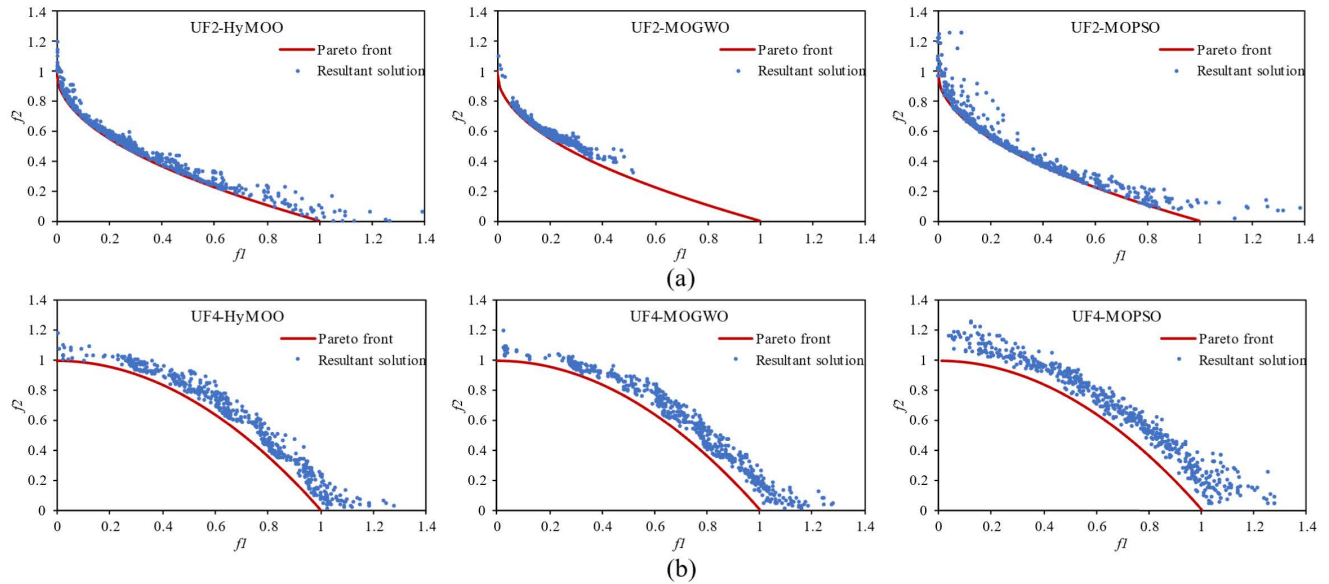
FIGURE 17. Resultant solutions of algorithms. (a) UF2. (b) UF4.

2) ALGORITHM PARAMETERS

The testing environment was chosen to be Python-3.9, and the device was an AMD Epyc-7601 32-core processor with 60GB of RAM.

For enabling the algorithm performance to be realistically represented by the actual parallel computing capabilities of the aforementioned environment under engineering problems, the test problems are in 6 dimensions. The populations are all set to 30 to approximate the maximum number of parallel calculations for CPU, and the maximum iteration number is 50 to reflect the convergence efficiency of the optimizer.

k and t_f act as important control factors for the EMOGWO algorithm in HyMOO and play a decisive role in regulating the convergence trend of the algorithm. During the preliminary preparation, several sets of replicate tests were carried out using different factor values, with UF2 and UF4 as benchmark functions. It was concluded that the robustness of the EMOGWO algorithm tends to increase and then decrease as k rises and reaches the best convergence success rate at $k = 5$. At the same time, an increase in t_f directly prolongs the lag time of convergence, and a relative optimum value of $t_f = 0.1$ is achieved after k is determined.

The relevant MOPSO parameters were set as: $c = 4$, $j = 10$ [25]. All parameters set for HyMOO and other candidates are shown in Table. 3.

3) PERFORMANCE VERIFICATION

20 independent calculations of each benchmark function were performed. The GD and IGD values of the test results are shown in Table. 4 and 5.

In UF2 benchmark, HyMOO has better GD and IGD values than the MOPSO algorithm. The MOGWO algorithm has a

TABLE 3. Parameters of testing algorithms.

Parameters	HyMOO	MOGWO	MOPSO
Population	20+10	30	30
t_{max}	50	50	50
σ	0.4	-	-
t_f	0.1	-	-
k	5	-	-
c	4	-	4
j	10	-	10

TABLE 4. GD of resultant solutions.

GD	UF2			UF4		
	HyMOO	MOGWO	MOPSO	HyMOO	MOGWO	MOPSO
Mean	0.01029	0.00416	0.02995	0.01416	0.01577	0.02291
Max	0.03260	0.01350	0.15430	0.01836	0.02088	0.02741
Min	0.00443	0.00120	0.00413	0.01457	0.01235	0.01814
Standard deviation	0.00623	0.00300	0.03776	0.00218	0.00215	0.00284
Variance	3.88e-05	8.81e-06	0.00143	4.77e-06	4.47e-06	8.08e-06

TABLE 5. IGD of resultant solutions.

IGD	UF2			UF4		
	HyMOO	MOGWO	MOPSO	HyMOO	MOGWO	MOPSO
Mean	0.006673	0.064474	0.007665	0.008481	0.009687	0.010926
Max	0.017327	0.080639	0.016604	0.010199	0.013683	0.014558
Min	0.003981	0.006602	0.004856	0.007546	0.006764	0.008236
Standard deviation	0.003329	0.016024	0.003555	0.000633	0.001986	0.001474
Variance	1.11e-05	2.568e-04	1.264e-05	4.01e-07	3.943e-06	2.172e-06

significant GD advantage, however, the IGD values are very poor, indicating that the algorithm may have trapped into local optimum several times during convergence, as verified in Fig. 17(a), which illustrates the distributions of resultant solutions from 20 tests of the three algorithms.

With the relatively more complex UF4 problem, both GD and IGD of HyMOO outperform the MOPSO and the MOGWO algorithm. The distributions of the resultant solutions are shown in Fig. 17(b), where the HyMOO results have

TABLE 6. Design parameters Set.

Parameters	Lower boundary	Upper boundary	Unit
w_m	4.5	7	mm
h_m	18	24	mm
h_{n1}	5	20	mm
h_{n2}	8	15	mm
h_{mo1}	1.5	4.5	mm
h_{mo2}	1	5.5	mm
α_1	9.5	19.2	deg
α_2	6.5	11.2	deg

FIGURE 19. Comparison of resultant solutions distribution from MOPSO.

FIGURE 18. Resultant solutions distribution from HyMOO.

FIGURE 20. Final design and prototype lamination.

TABLE 7. Comparison of optimal solutions.

Optimal solutions	I		II		III	
			Design specifications			
w_m	5.2		6		7	
h_m	23		22		24	
h_{n1}	1.5		2		2.6	
h_{n2}	8		9		10.7	
h_{mo1}	1.5		2.3		2.9	
h_{mo2}	2.1		1.1		2.2	
α_1	15.4		14.5		9.8	
α_2	6.6		14.0		9.3	
Calculated results	FE	MEC	FE	MEC	FE	MEC
Average Torque [Nm]	142.74	141.03	146.94	145.91	147.16	146.35
Torque ripple [%]	4.68	4.91	2.12	2.15	3.30	3.22

a good distribution and converge significantly better than the MOPSO algorithm.

In summary, HyMOO successfully inherits the advantages of the convergence speed of the original MOGWO algorithm and has good exploration ability and robustness. Under a limited computational resource, HyMOO can obtain more accurate optimization results in less time compared with MOPSO as well as the original MOGWO algorithm, which will be of great help to the optimization process and other practical engineering problems to be carried out below.

V. FAST DESIGN AND VERIFICATION
The proposed fast design method based on the MEC model and HyMOO is realized based on the specifications in Section II-IV.

The design parameters are calculated based on the requirements shown in Table 1 and the boundaries shown in Table 6 considering spatial constraints, pre-design calculations, and total material quality limit. The fast design process with FE and experimental validation are presented in the following subsections.

A. QUICK DESIGN AND RESULTANT SOLUTIONS
The corresponding parameters of the MEC model are first initialized in equal order based on the range of design parameters and the parallel calculation numbers. A 30-thread process of 50 iterations was executed in just 3:37:22, which is a significant computing speed advantage.
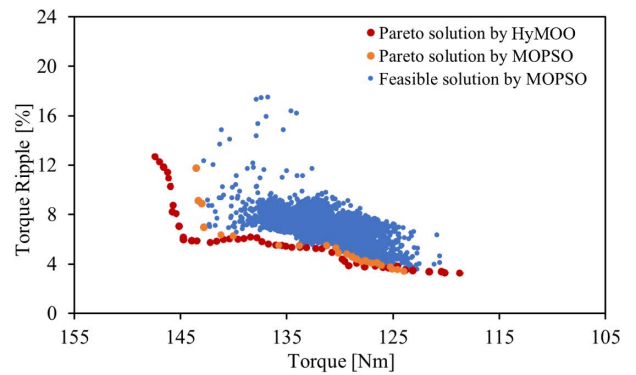
According to the calculated results in the present study average torque and torque ripple, the proposed HyMOO is used to find the optimal solution sets. The calculation results are shown in Fig. 18, where the Pareto solution sets are marked in red and are considered as the selection range for the optimal designs.

In addition, a computational comparison of the MOPSO algorithm under the same simulation environment and initial conditions needs to be mentioned in Fig. 19. It is easy to see that the conventional MOPSO algorithm runs into local optimal after the same converge iterations, which illustrate that MOPSO is no longer able to meet the requirements at
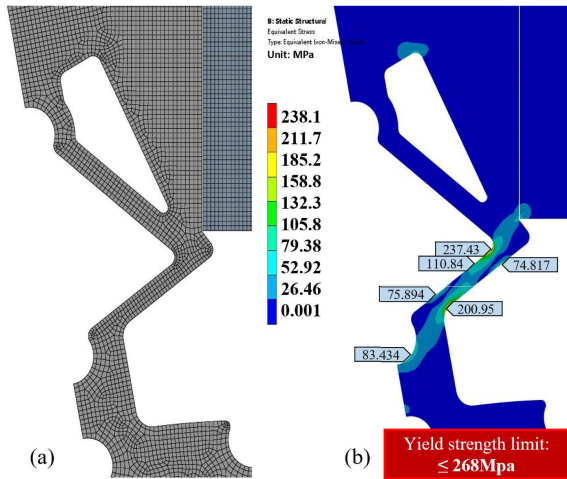
FIGURE 21. Mechanical analysis of final design. (a) Mesh used for FEA analysis. (b) Stress distribution in the rotor lamination at 6000 rpm.
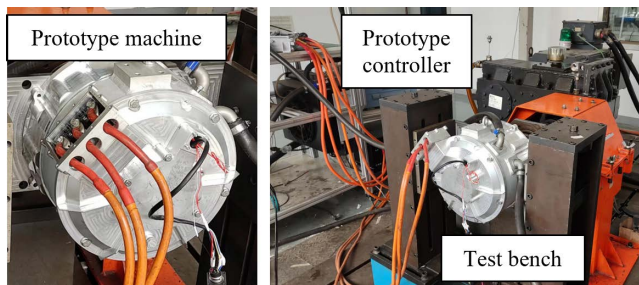

FIGURE 22. Prototype design and testing environment.

FIGURE 23. Back EMF comparison of MEC, FE, and experimental results.
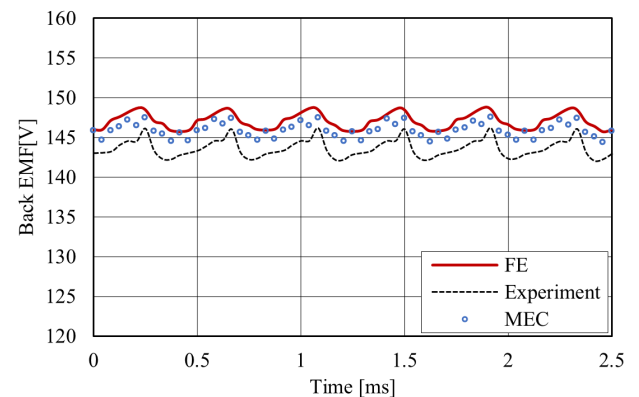
FIGURE 24. Output torque comparison of MEC, FE, and experimental results.

all in terms of optimization efficiency compared to the proposed HyMOO under a high-dimensional model of the actual problem.

Three sets of compliant design parameter values were selected from HyMOO results and fine-tuned to consider possible errors in the manufacturing process, recalculated by the MEC and FE models. The comparison results are shown in Table. 7.

In the three preferred designs, the MEC and FE calculations maintain a high level of agreement, with errors of less than 3% for average torque and less than 5% for torque ripple, proving that the solutions from the MEC model calculations can be accepted. Combining manufacturing cost and structural strength, Design II was chosen for the final solution.

B. PROTOTYPE VALIDATION

Based on Design II, lightening holes and stiffeners are properly designed without affecting the main magnetic circuit (Fig. 20).

A detailed mechanical analysis for rotor lamination is performed to make sure of the structure integrity. Fig. 21 shows the mesh of FEA mechanical analysis, and the result of stress distribution in the rotor lamination at the machine's maximum operating speed of 6000 rpm. It can be seen that the optimized rotor structure dose not exceed the yield strength limit of
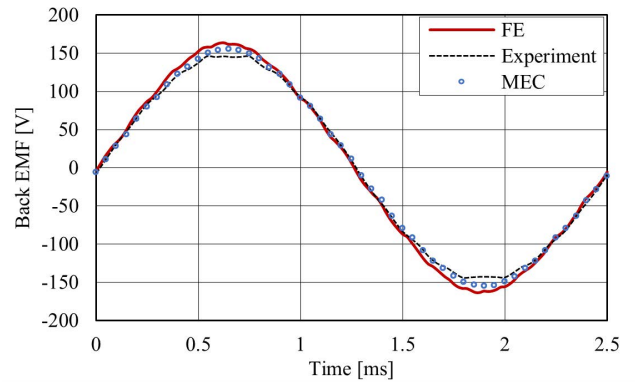
silicon steel material. Hence, the structural strength of final design meets the requirements of the machine's operating requirements.

A prototype FSCW spoke-type PM motor was built for experimental verification. The prototype and the testing rig are shown in Fig. 22.

Fig. 23 shows the experimental result of open-circuit line voltage waveform at 3000 rpm along with the calculation waveforms from MEC and FE model. The measured waveform looks quite good, and its value can be equated to 189.84V as DC voltage. The calculated line voltage equivalents are 191.69V in the MEC model and 194.75V in the FE model respectively, and the three waveforms are highly consistent as expected.

Fig. 24 shows the measured output torque curve from the prototype under 140Arms condition at 3000 rpm. According to the calculations, the average output torque of the prototype is 143.7Nm, which meets the design requirement of 140Nm; the torque ripple is 2.90%, which is less than the design requirement of 4.5%. Minor degradation in torque performance occurred, but the MEC model calculations proved to still be an accurate reference in the fast design, while the rated average torque and torque ripple of the prototype meets the design requirements. Besides, the measured efficiency
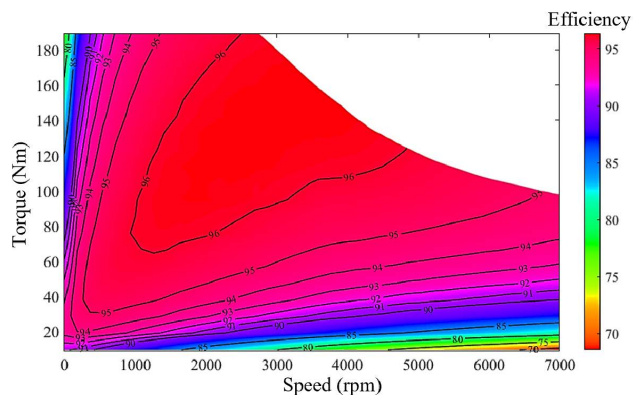
FIGURE 25. Measured efficiency map of prototype.

map in the speed range of 0 to 9,000 rpm are presented in Fig. 25. An ample high-efficiency zone is achieved for motor operating.

VI. CONCLUSION

In this article, a fast multi-objective analytical design for a spoke-type PM motor with AN structure is proposed based on lumped-parameter MEC and HyMOO. The MEC model is established according to 16-pole 18-slot FSCW motor topology, which is divided into 4 independent units, considering the core saturation effect and the influence of AN on air-gap flux density. The performance indices of air-gap flux density, flux linkage, back-EMF, cogging torque, torque output, as well as the processing time, are derived and validated by baseline FE model. Meanwhile, for better convergence speed and robustness, the HyMOO was developed based on the proposal EMOGWO, MOPSO, and random searching. The HyMOO is verified by benchmark tests, with much better efficiency than the original MOGWO and MOPSO. Finally, the fast multi-objective parametric design is adopted for the proposed motor prototype, using the MEC model as solver and HyMOO as optimizer, and the design requirements of 140Nm rated torque and 4.5% torque ripple are achieved.

It is found that MEC model can accurately reflect the influence of various parameters on the electromagnetic performance of the machine, and it takes only a very small calculation time compared with FE. At the same time, under the limited calculation process and iteration steps, HyMOO obtains a complete Pareto boundary based on MEC model as the solver. The analytical results of optimal designs match well with the FEM and prototype experimental results. The above multi-objective design and calculation process only takes less than 4 hours, and convincible electromagnetic parametric designs are obtained based on the initial motor topology, which shows great advantage in the multi-objective optimization in primary design stage of PM motor and shortens the design cycle of EV drive motor.

However, the limitation of using the proposed MEC model as a mathematical solver is obvious, that is, the MEC model is completely constrained by the corresponding motor

topology. Even if the MEC model is modular designed to adapt to different pole-slot combinations, how to establish a more general analytical model for PM motor is still the primary task of future research.

REFERENCES

[1] K. Urase, N. Yabu, K. Kiyota, H. Sugimoto, A. Chiba, M. Takemoto, S. Ogasawara, and N. Hoshi, "Energy efficiency of SR and IPM generators for hybrid electric vehicle," *IEEE Trans. Ind. Appl.*, vol. 51, no. 4, pp. 2874–2883, Jul. 2015, doi: 10.1109/TIA.2014.2387478.

[2] D. G. Dorrell, A. M. Knight, L. Evans, and M. Popescu, "Analysis and design techniques applied to hybrid vehicle drive machines— Assessment of alternative IPM and induction motor topologies," *IEEE Trans. Ind. Electron.*, vol. 59, no. 10, pp. 3690–3699, Oct. 2012, doi: 10.1109/TIE.2011.2165460.

[3] S. Saponara, C. H. T. Lee, N. X. Wang, and J. L. Kirtley, "Electric drives and power chargers: Recent solutions to improve performance and energy efficiency for hybrid and fully electric vehicles," *IEEE Veh. Technol. Mag.*, vol. 15, no. 1, pp. 73–83, Mar. 2020, doi: 10.1109/MVT.2019.2959343.

[4] Q. Chen, G. Xu, F. Zhai, and G. Liu, "A novel spoke-type PM motor with auxiliary salient poles for low torque pulsation," *IEEE Trans. Ind. Electron.*, vol. 67, no. 6, pp. 4762–4773, Jun. 2020, doi: 10.1109/TIE.2019.2924864.

[5] A. M. El-Refaie, "Fractional-slot concentrated-windings synchronous permanent magnet machines: Opportunities and challenges," *IEEE Trans. Ind. Electron.*, vol. 57, no. 1, pp. 107–121, Jan. 2010, doi: 10.1109/TIE.2009.2030211.

[6] M. Onsal, B. Cumhur, Y. Demir, E. Yolacan, and M. Aydin, "Rotor design optimization of a new flux-assisted consequent pole spoke-type permanent magnet torque motor for low-speed applications," *IEEE Trans. Magn.*, vol. 54, no. 11, pp. 1–5, Nov. 2018, doi: 10.1109/TMAG.2018.2832076.

[7] M. Kimiabeigi, R. Long, J. D. Widmer, and Y. Gao, "Comparative assessment of single piece and fir-tree-based spoke type rotor designs for low-cost electric vehicle application," *IEEE Trans. Energy Convers.*, vol. 32, no. 2, pp. 486–494, Jun. 2017, doi: 10.1109/TEC.2017.2662579.

[8] J. H. Lee, J.-Y. Song, D.-W. Kim, J.-W. Kim, Y.-J. Kim, and S.-Y. Jung, "Particle swarm optimization algorithm with intelligent particle number control for optimal design of electric machines," *IEEE Trans. Ind. Electron.*, vol. 65, no. 2, pp. 1791–1798, Feb. 2018, doi: 10.1109/TIE.2017.2760838.

[9] A. Fatemi, D. M. Ionel, M. Popescu, Y. C. Chong, and N. A. O. Demerdash, "Design optimization of a high torque density spoke-type PM motor for a formula E race drive cycle," *IEEE Trans. Ind. Appl.*, vol. 54, no. 5, pp. 4343–4354, Sep. 2018, doi: 10.1109/TIA.2018.2844804.

[10] G. J. Li, Z. Q. Zhu, M. Foster, and D. Stone, "Comparative studies of modular and unequal tooth PM machines either with or without tooth tips," *IEEE Trans. Magn.*, vol. 50, no. 7, pp. 1–10, Jul. 2014, doi: 10.1109/TMAG.2014.2310179.

[11] L. Jolly, M. A. Jabbar, and L. Qinghua, "Design optimization of permanent magnet motors using response surface methodology and genetic algorithms," *IEEE Trans. Magn.*, vol. 41, no. 10, pp. 3928–3930, Oct. 2005, doi: 10.1109/TMAG.2005.854966.

[12] K. Sun and S. Tian, "Multiobjective optimization of IPMSM with FSCW applying rotor notch design for torque performance improvement," *IEEE Trans. Magn.*, vol. 58, no. 5, pp. 1–9, May 2022, doi: 10.1109/TMAG.2022.3155269.

[13] C. Wu and M. Hamada, "Response surface methodology," in *Experiments: Planning, Analysis, and Optimization*, 3rd ed. Hoboken, NJ, USA: Wiley, 2021, ch. 10.

[14] G. Liu, Y. Wang, Q. Chen, G. Xu, and C. Song, "Multiobjective deterministic and robust optimization design of a new spoke-type permanent magnet machine for the improvement of torque performance," *IEEE Trans. Ind. Electron.*, vol. 67, no. 12, pp. 10202–10212, Dec. 2020, doi: 10.1109/TIE.2019.2962472.

[15] J.-G. Lee, D.-K. Lim, and H.-K. Jung, "Analysis and design of interior permanent magnet synchronous motor using a sequential-stage magnetic equivalent circuit," *IEEE Trans. Magn.*, vol. 55, no. 10, pp. 1–4, Oct. 2019, doi: 10.1109/TMAG.2019.2922043.

[16] S. Li, W. Tong, M. Hou, S. Wu, and R. Tang, "Analytical model for no-load electromagnetic performance prediction of V-shape IPM motors considering nonlinearity of magnetic bridges," *IEEE Trans. Energy Convers.*, vol. 37, no. 2, pp. 901–911, Jun. 2022, doi: 10.1109/TEC.2021.3121438.

[17] X. Kong, Y. Hua, Z. Zhang, C. Wang, and Y. Liu, "Analytical modeling of high-torque-density spoke-type permanent magnet in-wheel motor accounting for rotor slot and eccentric magnetic pole," *IEEE Trans. Transp. Electrific.*, vol. 7, no. 4, pp. 2683–2693, Dec. 2021, doi: 10.1109/TTE.2021.3078449.

[18] H. Moslemi and M. Zandieh, "Comparisons of some improving strategies on MOPSO for multi-objective (r, Q) inventory system," *Expert Syst. Appl.*, vol. 38, no. 10, pp. 12051–12057, Sep. 2011, doi: 10.1016/j.eswa.2011.01.169.

[19] S. Wu, L. Guo, H. Wang, Z. Wang, Z. Song, and T. Shi, "Analytical calculation for magnetic field in spoke-type permanent magnet machines based on a rotor magnetic potential model," *IEEE Trans. Magn.*, vol. 58, no. 2, pp. 1–5, Feb. 2022, doi: 10.1109/TMAG.2021.3077917.

[20] H. Chen, X. Liu, A. M. EL-Refaie, J. Zhao, N. A. O. Demerdash, and J. He, "Comparative study of winding configurations of a five-phase flux-switching PM machine," *IEEE Trans. Energy Convers.*, vol. 34, no. 4, pp. 1792–1804, Dec. 2019, doi: 10.1109/TEC.2019.2921891.

[21] J. K. Tangudu, T. M. Jahns, and A. EL-Refaie, "Core loss prediction using magnetic circuit model for fractional-slot concentrated-winding interior permanent magnet machines," in *Proc. IEEE Energy Convers. Congr. Expo.*, Atlanta, GA, USA, Sep. 2010, pp. 1004–1011, doi: 10.1109/ECCE.2010.5617873.

[22] S.-H. Han, T. M. Jahns, and W. L. Soong, "A magnetic circuit model for an IPM synchronous machine incorporating moving airgap and cross-coupled saturation effects," in *Proc. IEEE Int. Electr. Mach. Drives Conf.*, May 2007, pp. 21–26, doi: 10.1109/IEMDC.2007.383546.

[23] D. A. Vanveldhuizen and G. B. Lamont, "Evolutionary computation and convergence to a Pareto front," in *Proc. 3rd Annu. Genetic Program. Conf.*, 1998, pp. 221–228.

[24] Q. Zhang, W. Liu, and H. Li, "The performance of a new version of MOEA/D on CEC09 unconstrained MOP test instances," in *Proc. IEEE Congr. Evol. Comput.*, Trondheim, Norway, May 2009, pp. 203–208, doi: 10.1109/CEC.2009.4982949.

[25] Y. Zhang, D.-W. Gong, and Z. Ding, "A bare-bones multi-objective particle swarm optimization algorithm for environmental/economic dispatch," *Inf. Sci.*, vol. 192, no. 1, pp. 213–227, Jun. 2012, doi: 10.1016/j.ins.2011.06.004.

[26] S. Mirjalili, S. M. Mirjalili, and A. Lewis, "Grey wolf optimizer," *Adv. Eng. Softw.*, vol. 69, pp. 46–61, Mar. 2014, doi: 10.1016/j.advengsoft.2013.12.007.

[27] S. Mirjalili, S. Saremi, S. M. Mirjalili, and L. D. S. Coelho, "Multiobjective grey wolf optimizer: A novel algorithm for multi-criterion optimization," *Expert Syst. Appl.*, vol. 47, pp. 106–119, Apr. 2016, doi: 10.1016/j.eswa.2015.10.039.

[28] A. Sahoo and S. Chandra, "Multi-objective grey wolf optimizer for improved cervix lesion classification," *Appl. Soft Comput.*, vol. 52, pp. 64–80, Mar. 2017, doi: 10.1016/j.asoc.2016.12.022.

[29] M. Zhang, D.-L. Yin, X.-L. Yang, and Q. Yang, "Improved grey wolf algorithm based on nonlinear control parameter combination strategy," *Comput. Appl. Softw.*, vol. 38, no. 5, pp. 250–255 and 322, 2021.

[30] Q. Zhang, A. Zhou, S. Z. Zhao, P. N. Suganthan, W. Liu, and S. Tiwari, "Multiobjective optimization test instances for the CEC-2009 special session and competition," 2008. [Online]. Available: http://www.ntu.edu.sg/home/epnsugan/

[31] D. A. Vanveldhuizen and G. B. Lamont, "Evolutionary computation and convergence to a Pareto front," in *Proc. 3rd Annu. Genetic Program. Conf.*, 1998, pp. 22–25.

[32] P. A. N. Bosman and D. Thierens, "The balance between proximity and diversity in multiobjective evolutionary algorithms," *IEEE Trans. Evol. Comput.*, vol. 7, no. 2, pp. 174–188, Apr. 2003, doi: 10.1109/TEVC.2003.810761.

CONGDA XIAO received the B.Sc. degree in automation from Chang'an University, Xi'an, China, in 2020. He is currently pursuing the M.Sc. degree in energy power engineering with the School of Automotive Engineering, Wuhan University of Technology, Wuhan, China.

His research interests include PM machine design and optimization of EV drive unit control.

AIGUO HAN received the M.Sc. degree in mechanical manufacturing and automation from Jilin University, Jilin, China, in 2001, and the Ph.D. degree in mechatronics engineering from the Huazhong University of Science and Technology, Wuhan, China, in 2008.

He has been with the Wuhan University of Technology, Wuhan, since 2008; and an Associate Professor at the School of Automotive Engineering, since 2013. His research interests include the control of EV drive systems, measuring and testing techniques of electric drive unit, and optimization of electrical machines.

WENLONG XIE received the M.Sc. degree in electrical engineering from the Tianjin University of Technology, Tianjin, China, in 2020. He is currently working as a Electromagnetic Engineer at the Foshan Xianhu Laboratory of the Advanced Energy Science and Technology Guangdong Laboratory, Foshan, China.

His research interests include motor design and state identification of switched reluctance motor.

MINQI HE received the B.Sc. degree in automotive engineering from Chang'an University, Xi'an, China, in 2021. She is currently pursuing the M.Sc. degree in automotive engineering with the School of Automotive Engineering, Wuhan University of Technology, Wuhan, China.

Her research interests include machine learning and advance manufacturing technology.

. . .